JOURNAL OF GEOPHYSICAL RESEARCH, VOL. 107, NO. A10, 1320, doi:10.1029/2002JA009259, 2002

Evidence for Langmuir wave tunneling in the inhomogeneous solar wind

A. J. Willes
School of Physics, University of Sydney, Sydney, New South Wales, Australia

S. D. Bale
Space Sciences Laboratory, University of California, Berkeley, California, USA

Iver H. Cairns
School of Physics, University of Sydney, Sydney, New South Wales, Australia

Received 13 January 2002; revised 12 April 2002; accepted 15 May 2002; published 23 October 2002.

[1] Spacecraft observations of beat-like Langmuir waveforms on two orthogonal antennas in Earth's foreshock and the solar wind have been interpreted as beating associated with large-angle reflection of Langmuir waves from density inhomogeneities or nonlinear decay processes. However, the waveforms are often irregular, with uncorrelated waveform envelopes on orthogonal antennas. One interpretation is that irregular waveforms are a manifestation of the electromagnetic nature of Langmuir waves scattered to low wave numbers in the inhomogeneous solar wind. An alternative interpretation, investigated here, is that the shape of the waveform envelopes on orthogonal antennas becomes substantially different as Langmuir waves tunnel through evanescent regions, where the local plasma frequency in the inhomogeneous plasma exceeds the Langmuir wave frequency. We demonstrate that observations of uncorrelated waveform envelopes on orthogonal antennas are consistent with theoretical predictions for Langmuir wave tunneling in evanescent regions in the inhomogeneous solar wind. Incident Langmuir waves which are nearly aligned with the density gradient are also partially converted to transverse electromagnetic waves at the plasma frequency. The characteristic dual-antenna waveform signature of mode conversion is difficult to detect for typical solar wind parameters. *INDEX TERMS:* 2164 Interplanetary Physics: Solar wind plasma; 7534 Solar Physics, Astrophysics, and Astronomy: Radio emissions; 2159 Interplanetary Physics: Plasma waves and turbulence; 2154 Interplanetary Physics: Planetary bow shocks; *KEYWORDS:* Langmuir waves, tunneling, density inhomogeneities

Citation: Willes, A. J., S. D. Bale, and I. H. Cairns, Evidence for Langmuir wave tunneling in the inhomogeneous solar wind, *J. Geophys. Res.*, *107*(A10), 1320, doi:10.1029/2002JA009259, 2002.

1. Introduction

[2] Langmuir waves in the solar wind and planetary foreshocks are generated by fast electron beams via the bump-in-tail instability. For typical beam speeds and widths, Langmuir waves are predicted to be electrostatic and quasi-monochromatic [e.g., *Filbert and Kellogg*, 1979; *Cairns*, 1987; *Robinson et al.*, 1993b]. However, Langmuir wave events in the solar wind and Earth's foreshock measured by the Time Domain Sampler (TDS) instrument on the Wind spacecraft, which simultaneously samples electric field waveforms on two orthogonal antennas with high time resolution, are not always consistent with quasi-monochromatic Langmuir waves. Instead, the waveform envelopes on the two antennas are often substantially different, and the relative phase between the two carrier signals often drifts substantially over the 17 ms sample time of each TDS event [*Bale et al.*, 1998; *Kellogg et al.*, 1999]. In contrast, quasi-monochromatic electrostatic Langmuir waves are expected to produce similar signals on orthogonal antennas, with zero (or π) relative phase shift. Various effects proposed to interpret these observations include: (i) electromagnetic properties of Langmuir waves shifted to low wave numbers in an inhomogeneous, weakly magnetized plasma [*Bale et al.*, 1998; *Willes and Cairns*, 2000], (ii) beating between incident and reflected Langmuir waves at density gradients [*Kellogg et al.*, 1999], and (iii) beating between primary and backscattered Langmuir waves from nonlinear electrostatic decay [*Cairns and Robinson*, 1992b]. These interpretations are not necessarily contradictory.

[3] The aim of this paper is to investigate two alternative interpretations: Langmuir wave tunneling in evanescent regions where the local plasma frequency exceeds the Langmuir wave frequency [*Kellogg*, 1986; *Kellogg et al.*, 1999], and mode conversion of Langmuir waves propagat-

0148-0227/02/2002JA009259$09.00

ing nearly parallel to the density gradient [*Field*, 1956; *Willes and Cairns*, 2001]. Both of these effects are associated with density inhomogeneities in the ambient plasma. Additional evidence for density inhomogeneities being important in this context is provided by the success of stochastic growth theory in describing Langmuir electric field statistics in type III sources and Earth's foreshock [*Robinson et al.*, 1993a; *Cairns and Robinson*, 1999].

[4] Beat-like Langmuir waveforms have previously been observed with high time resolution on one antenna by the Voyager and Galileo spacecraft in type III-associated events in the solar wind at 1 AU [*Gurnett et al.*, 1993] and in the foreshocks of Venus [*Hospodarsky et al.*, 1994] and Jupiter [*Gurnett et al.*, 1981] and interpreted as evidence for Langmuir wave decay, with beating between parent and backscattered Langmuir waves [*Cairns and Robinson*, 1992b]. In accordance with the above mentioned Wind observations, the Voyager and Galileo waveforms are often irregular (i.e., not beat-like), often consisting of one or more solitary Langmuir wave packets. Wave packet localization due to strong turbulence processes can be ruled out because of the low Langmuir wave fields present [*Cairns and Robinson*, 1992a, 1995; *Gurnett et al.*, 1993; *Bale et al.*, 1997]. An alternative interpretation is that the irregular Langmuir waveforms are produced as a consequence of a nonlinear interaction between beam electrons and growing Langmuir waves [*Muschietti et al.*, 1995, 1996].

[5] *Willes and Cairns* [2001] investigated Langmuir wave reflection and mode conversion at density gradients, following the approach of *Forslund et al.* [1975] and *Means et al.* [1981], by numerically solving the wave equations in a warm unmagnetized plasma for Langmuir waves approaching a linear density gradient from a constant-density region. The main advantage of the numerical approach is that it yields exact solutions for the wave fields, in contrast to more approximate analytic solutions based on perturbative methods [e.g., *Hinkel-Lipsker et al.*, 1992; *Yin and Ashour-Abdalla*, 1999], where the wave field solutions are valid only very close to the mode conversion point. *Willes and Cairns* [2001] demonstrated that higher mode conversion efficiencies are possible than previously calculated, but in a more restricted region of parameter space. The same numerical approach is used in this paper, with the important modification that the linear density gradient is replaced with a more physically realistic density profile generated from measured solar wind density power spectra. This permits Langmuir wave tunneling to be investigated in addition to Langmuir wave reflection and mode conversion.

[6] This paper is organized as follows: the theoretical formalism is introduced in section 2, with an outline of the method for obtaining the model plasma density profile and wave equations. In section 3, Langmuir waveforms are generated in the total reflection regime, in which all of the incident Langmuir wave energy is eventually reflected over a number of spatially separated reflection points where the local plasma frequency equals the Langmuir wave frequency. At each reflection point, Langmuir waves tunnel through (narrow) evanescent regions where the plasma frequency exceeds the wave frequency. We demonstrate that observed irregular Langmuir waveforms on orthogonal antennas are consistent with Langmuir wave tunneling in evanescent regions. In section 4, we consider the mode conversion regime, where incident Langmuir waves are nearly aligned with the density gradient, and a fraction of incident Langmuir waves are converted to transverse waves, in addition to reflected Langmuir waves. It is shown that the characteristic dual-antenna signature of mode conversion events is difficult to detect in practice.

2. Theoretical Model

2.1. Plasma Density Profile

[7] In order to study Langmuir wave tunneling, in addition to Langmuir wave reflection and mode conversion, we generate a model plasma density profile, which is statistically similar to measured density inhomogeneities in the solar wind. This is achieved by inverting measured solar wind density power spectra, using the method described by *Kellogg et al.* [1999]. The assumed power spectrum is obtained from solar wind data [*Unti et al.*, 1973], with [*Kellogg et al.*, 1999],

$$P = 5 \times 10^{-3} f^{-1.54}. \qquad (1)$$

Synthetic density time series are calculated by inverse transforming the Fourier series, after assigning a random phase to each Fourier component. We extrapolate the power law from the upper frequency of 13 Hz measured by *Unti et al.* [1973] up to 100 Hz. Despite the fact that this introduces finer detail into the model density time profile, we stress that variation of the upper-frequency cutoff of the power spectrum will not significantly affect the conclusions presented here. The upper portion of Figure 1 shows a section (0.4 seconds) of one density time series (10 seconds) generated by this method.

[8] Electron-beam-generated Langmuir waves in the solar wind have frequencies just above the local plasma frequency ω_p, and higher beam speeds yield lower Langmuir wave frequencies (closer to ω_p). In a fluctuating density profile propagating Langmuir waves frequently encounter evanescent regions where the local plasma frequency exceeds the Langmuir wave frequency. This is illustrated in Figure 1, where incident Langmuir waves (at relative frequency labeled ω_L in Figure 1) freely propagate in regions marked by the dashed line. At the first reflection point (where $\omega_L = \omega_p$, near $t = 0.14$), Langmuir waves are reflected, converted into transverse electromagnetic waves (depending on the incidence angle, as discussed in section 3), or tunnel through the evanescent region (dotted line) to the next region where they can freely propagate. At the final reflection point ($t \gtrsim 0.18$), the Langmuir waves encounter a density ramp, through which only an infinitesimal fraction of incident Langmuir wave energy will penetrate. Thus, all of the transmitted Langmuir wave energy is reflected at this final reflection point.

2.2. Wave Equations

[9] The wave equation derivation closely follows similar derivations in *Forslund et al.* [1975], *Means et al.* [1981], and *Willes and Cairns* [2001], with the essential difference that the simplifying assumption of a linear density gradient is relaxed. Numerical solutions of these wave equations for the model density profile in Figure 1 facilitate the following discussion of Langmuir wave reflection, tunneling and

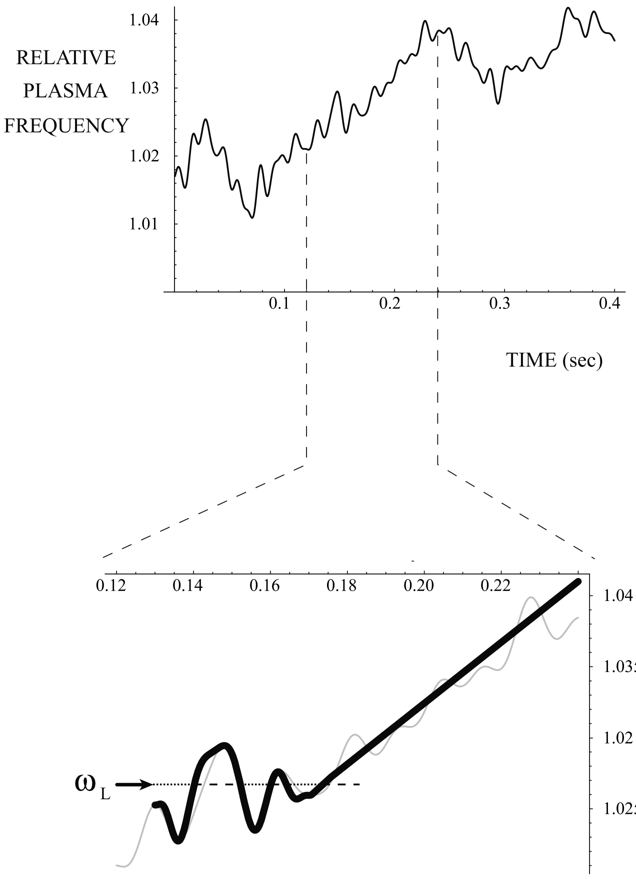

Figure 1. Plasma density time series generated from measured solar wind density power spectra. Incoming Langmuir waves (frequency ω_L) tunnel through two evanescent regions before being totally reflected at the third (density ramp).

mode conversion in sections 3 and 4. The following assumptions are made to simplify the analysis:

1. The density gradient is one-dimensional. Without loss of generality, we define the coordinate system in the rest frame of the solar wind plasma such that the density gradient ∇n is in the positive X direction, and the wave electric field vector $\mathbf{E}$ lies in the X–Y plane, and can be expressed in the form $E(\mathbf{X}, t) = [E_X(X), E_Y(X), 0] \exp[i\,(K_Y Y - \omega t)]$, where spatial variables are expressed in dimensionless form using $X = k_0 x$, $Y = k_0 y$, $K = k/k_0$, and $k_0 = \omega/c$, where ω is the wave frequency and c is the speed of light. Here $K_Y = k_Y/k_0$ is constant by Snell's law. We seek steady state solutions for the wave fields, with constant ω. The assumed density profile is illustrated in Figure 2, where the dimensionless plasma density $N(X) = \omega_p^2(X)/\omega^2 \propto n$, for plasma frequency ω_p and (constant) incident Langmuir wave frequency ω. The model density profile in Figure 2 is taken from a smoothed section of the density time series in Figure 1 (bold line), where the time axis is converted to distance by assuming that the slowly evolving density structure is convected past the spacecraft at the solar wind speed (assuming $v_{sw} = 400$ km s^{-1}). Constant plasma density is assumed for $X \leq 0$, with the constant value N_0 (= 0.996 in Figure 2) dependent on the plasma and beam parameters. We assume that Langmuir waves approach from the constant-density region ($X < 0$) toward the inhomogeneous region ($X > 0$).

2. The plasma is unmagnetized with no background flows; i.e., $\mathbf{u}_0 = 0$ and $\mathbf{B}_0 = 0$, where $\mathbf{u}(\mathbf{X}, t)$ is the electron fluid velocity (the ions are static), $\mathbf{E}(\mathbf{X}, t)$ and $\mathbf{B}(\mathbf{X}, t)$ are the wave electric and magnetic fields, and subscripts 0 and 1 refer to unperturbed and perturbed quantities, respectively.

3. The plasma obeys an adiabatic pressure law, with $pn^{-\gamma}$ = constant, where $p(\mathbf{X}, t)$ is the plasma pressure, $n(\mathbf{X}, t)$ is the electron density, and γ is the ratio of specific heats. For small perturbations, $p_0 = n_0 T$, and $p_1 = \gamma\, n_1 p_0/n_0$, where T is the electron temperature.

4. Wave damping is negligible.

[10] The wave equation is obtained by linearizing Maxwell's equations and the electron momentum equation [e.g., *Willes and Cairns*, 2001], with

$$\nabla^2\mathbf{E}_1 - \nabla(\nabla\cdot\mathbf{E}_1) + \{1 - N(X)\}\mathbf{E}_1 - \beta\left\{-\gamma\nabla(\nabla\cdot\mathbf{E}_1) + (\nabla\cdot\mathbf{E}_1)\frac{N'(X)}{N(X)}\right\} = 0, \tag{2}$$

where $N(X) = \omega_p(X)^2/\omega^2$, and $\beta = T_e/m_e c^2$. The X and Y components of this wave equation yield two coupled second-order linear differential equations for $E_X(X)$ and $E_Y(X)$ (which are related to the total field by $\mathbf{E}_1(\mathbf{X}) = [E_X(X), E_Y(X), 0] \exp[iK_Y Y]$):

$$\gamma\beta E_X'' - iK_Y(1-\gamma\beta)E_Y' + \left(1 - N(X) - K_Y^2\right)E_X = \beta\frac{N'(X)}{N(X)} \cdot \left(E_X' + iK_Y E_Y\right), \tag{3}$$

$$E_Y'' - iK_Y(1-\gamma\beta)E_X' + \left(1 - N(X) - \gamma\beta K_Y^2\right)E_Y = 0. \tag{4}$$

These equations reduce to the equations in *Willes and Cairns* [2001] by replacing the term $N'(X)/N(X)$ with $1/L$ for a linear density gradient with scale length L.

[11] Reflection and/or mode conversion occurs at points X_{ref} where $N(X_{\text{ref}}) = 1$. The boundary conditions are determined as follows. For $X < 0$, $\omega_p(X) = \omega_{p0}$ is constant and $E_Y(X)$ can be expressed as the sum of three plane waves:

$$E_Y(X) = \exp(iK_{LX}X) + R_L\exp(-iK_{LX}X) + T_T\exp(-iK_{TX}X), \tag{5}$$

where the first term corresponds to an incoming Langmuir wave, and K_{LX} is the X component of the dimensionless

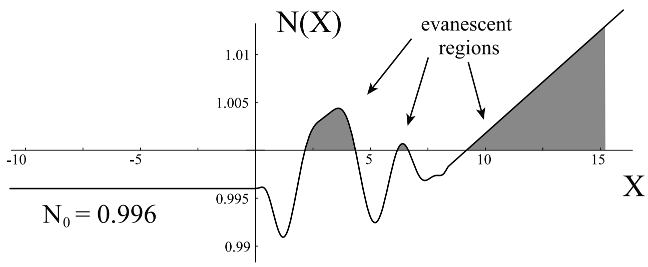

Figure 2. Model plasma density profile, with $N(X) \propto \omega_p^2/\omega_L^2$, which is constant for $X < 0$, and variable for $X > 0$, with functional dependence taken from the density time series in Figure 1 (bold line). Evanescent regions (shaded) correspond to where $\omega_L \leq \omega_p$.

Langmuir wave vector, satisfying the Langmuir wave dispersion relation

$$K_{LX}^2 = \frac{1 - N_0}{\gamma\beta} - K_Y^2. \tag{6}$$

The second term in equation (5) corresponds to a reflected Langmuir wave, where R_L is the (complex) Langmuir wave reflection coefficient. The third term corresponds to the mode-converted transverse wave, which propagates away from the mode-coupling region in the negative X-direction, where K_{TX} is the X-component of the dimensionless transverse wave vector, satisfying the transverse wave dispersion relation

$$K_{TX}^2 = 1 - N_0 - K_Y^2, \tag{7}$$

and T_T is the (complex) mode-conversion coefficient.

[12] The angle θ_L between the incoming Langmuir wave and the density gradient, at the interface between the constant and varying density regions ($X = 0$) is

$$\sin^2\theta_L = \frac{\gamma\beta K_Y^2}{1 - N_0}. \tag{8}$$

The angle θ_T between the transverse wave and the density gradient at $X = 0$ is

$$\sin^2\theta_T = \frac{K_Y^2}{1 - N_0}. \tag{9}$$

[13] An expression for $E_X(X)$ analogous to equation (5) is obtained using the relations $\nabla \times \mathbf{E}_{long} = 0$ and $\nabla \cdot \mathbf{E}_{trans} = 0$, where $\mathbf{E}_{long}$ is the longitudinal part of $\mathbf{E}$ (Langmuir waves) and $\mathbf{E}_{trans}$ is the transverse part of $\mathbf{E}$ (transverse EM waves), with

$$E_X(X) = \frac{K_{LX}}{K_Y}[\exp(iK_{LX}X) - R_L\exp(-iK_{LX}X)] + \frac{K_Y}{K_{TX}}T_T\exp(-iK_{TX}X). \tag{10}$$

From equations (5) and (10), the coefficients R_L and T_T can be expressed in terms of the fields at $X = 0_-$, yielding [*Means et al.*, 1981],

$$R_L = \frac{K_{TX}K_Y}{K_{LX}K_{TX} + K_Y^2}\left[-E_X(0_-) + \frac{K_Y}{K_{TX}}E_Y(0_-) + \frac{K_{LX}}{K_Y} - \frac{K_Y}{K_{TX}}\right], \tag{11}$$

$$T_T = \frac{K_{TX}K_Y}{K_{LX}K_{TX} + K_Y^2}\left[E_X(0_-) + \frac{K_{LX}}{K_Y}E_Y(0_-) - 2\frac{K_{LX}}{K_Y}\right]. \tag{12}$$

[14] Boundary conditions for the derivatives of E_X and E_Y are then obtained by differentiating the expressions (5) and (10) and evaluating them at $X = 0_-$:

$$\frac{dE_X(0_-)}{dX} = i\left[\frac{K_{LX}^2}{K_Y}(1 + R_L) - K_Y T_T\right], \tag{13}$$

$$\frac{dE_Y(0_-)}{dX} = i[K_{LX}(1 - R_L) - K_{TX}T_T]. \tag{14}$$

The other boundary conditions are that the wave fields decay to zero beyond the final reflection point; i.e.,

$$E_X(X_\infty) = E_Y(X_\infty) = 0, \tag{15}$$

where $X_\infty \gg \max\{X_{\mathrm{ref}}\}$. The differential equations (3) and (4) with boundary conditions (13), (14), and (15) are solved numerically as a boundary value problem, using an adaptive shooting method, with $E_X(0)$ and $E_Y(0)$ as the undetermined parameters.

3. Langmuir Wave Reflection and Tunneling

[15] Langmuir waves incident on an increasing density gradient are totally reflected when they are not closely aligned with the density gradient (i.e., no incident Langmuir wave energy is converted to transverse electromagnetic waves). Equations (8) and (9) impose a maximum angle $\theta_{L\max}$ between the Langmuir wave and the density gradient for mode conversion to occur; i.e., $\sin^2\theta_T \leq 1$ implies that $K_Y^2/(1-N_0) \leq 1$, so that

$$\theta_{L\max} = \sin^{-1}\sqrt{\gamma\beta}. \tag{16}$$

For $\theta_L \geq \theta_{L\max}$, no transverse waves are generated and incident Langmuir waves are totally reflected (either before, or at the final reflection point). In this case, $T_T = 0$ in equations (5) and (10), and the boundary conditions (13) and (14) are replaced with

$$\frac{dE_X(0_-)}{dX} = i\frac{K_{LX}^2}{K_Y}(1 + R_L), \tag{17}$$

$$\frac{dE_Y(0_-)}{dX} = iK_{LX}(1 - R_L), \tag{18}$$

for the reflection coefficient $R_L = E_Y(0_-) - 1$.

[16] *Kellogg et al.* [1999] interpreted the modulation of observed Langmuir waveform envelopes as beating between incident and reflected Langmuir waves; the latter are a product of density inhomogeneities in the solar wind. For large reflection angles, the Doppler frequency shift between incident and reflected waves in the spacecraft frame differs when their wave vectors have different orientations relative to the solar wind direction. Strong evidence for wave beating due to the solar wind Doppler shift is presented in the TDS event in Figure 8 of *Kellogg et al.* [1999], where the frequency difference between the two distinct peaks in the power spectrum corresponds to the modulation (beat) frequency. Another property of beating between incident and reflected waves is that local envelope maxima on one antenna correlate with local envelope minima on an orthogonal antenna (irrespective of spacecraft orientation). This is evident over several envelope oscillations in Figure 3 (the same event as Figure 8 in *Kellogg et al.* [1999]). For instance, at times A and B, there is a correspondence between local envelope maxima and minima on the two antennas. However, at later times this correspondence breaks down; for example, at times C and D.

[17] We generate simulated waveforms for comparison with the Wind TDS events, assuming that incident beam-

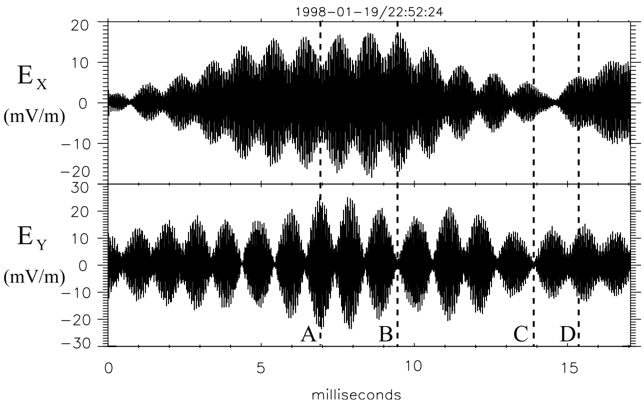

Figure 3. Measured electric fields on the (orthogonal) X and Y antennas of the TDS instrument on the Wind spacecraft. The modulated envelope maxima and minima are correlated on the X and Y antennas at times A and B, but not at times C and D.

generated Langmuir waves (parameters: $\beta = 4 \times 10^{-5}$, $V_e = 1.9 \times 10^6$ m s^{-1}, $\omega_{p0} = 1.5 \times 10^5$ m s^{-1}, $\gamma = 3$, $v_{beam} = 5.2 \times 10^7$ m s^{-1}, and incidence angle $\theta = 0.186$ rad) encounter the model density profile shown in Figure 1. For these parameters, the Debye length on the dimensionless spatial scale is 6.3×10^{-3}, and $N_0 = (1 + 3V_e^2/v_b^2)^{-1} = 0.996$ in the constant density region ($X < 0$). The incidence angle well exceeds the critical reflection angle, with $\theta_L \gg \theta_{L\ \max} = 0.011$ rad. Hence there is no mode conversion, and the Langmuir waves are totally reflected.

[18] Figure 4 displays the (steady state) solutions for the electric field components E_X and E_Y of the wave equations (3) and (4), with boundary conditions (17) and (18), for the model density profile in Figure 2. The waves are evanescent (exponentially decaying) in regions where $g(X) > 1$ in Figure 2, and the wave electric field approaches zero in the final evanescent region (at the density ramp, for $X > 9$).

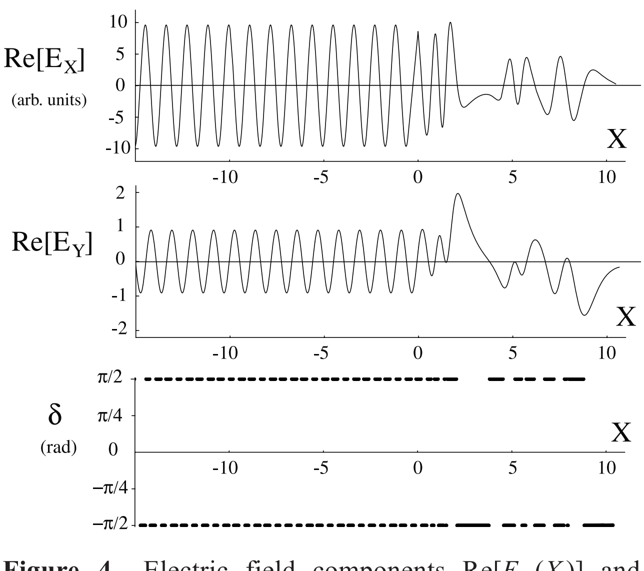

Figure 4. Electric field components Re[$E_X(X)$] and Re[$E_Y(X)$], and the relative phase $\delta(X) = \tan^{-1}$[Re($E_Y(X)/E_X(X)$), Im($E_Y(X)/E_X(X)$)] for incident Langmuir wave angle $\theta = 0.186$ rad (other parameters are given in text).

In order to generate Langmuir waveforms for comparison with Wind TDS observations, we assume a straight-line spacecraft trajectory in the solar wind rest frame, with

$$X(t) = X_0 + \sin\theta_{sc}\cos\phi_{sc}\, v_{sw} t \tag{19}$$

$$Y(t) = Y_0 + \sin\theta_{sc}\sin\phi_{sc}\, v_{sw} t \tag{20}$$

where (X_0, Y_0) is the spacecraft position at $t = 0$, and the polar angles θ_{sc} and ϕ_{sc} define the direction of spacecraft motion (with speed $v_{sw} = 400$ km s^{-1}) relative to the density gradient. We also assume that the X-antenna is aligned with the density gradient. The "measured" electric field has the form

$$\mathbf{E}(t) = \mathrm{Re}\{(E_X[X(t)], E_Y[X(t)], 0)\exp[i(K_Y Y(t) - \omega t)]\}. \tag{21}$$

[19] Figure 5 shows components of the electric field $\mathbf{E}(t)$ on the X and Y antennas for $E(X)$ and $E(Y)$ from Figure 4, $X_0 = -1$, $Y_0 = 0$, $\theta_{sc} = \pi/8$, and $\phi_{sc} = \pi/16$. We make an arbitrary choice for the polar trajectory angles θ_{sc} and ϕ_{sc} to exclude the special case where the spacecraft travels along the density gradient. For $\theta_{sc} = \pi/8$, the spacecraft travels nearly perpendicular to the density gradient. One effect of varying θ_{sc} toward $\pi/2$ (with $\phi_{sc} \approx 0$, so that the spacecraft travels along the density gradient) would be an increase in the measured beat frequency (with more Langmuir wave packets present over the time interval displayed in Figure 5).

[20] The vertical lines (A, B, C and D) highlight the correlation between envelope maxima and minima on the X and Y antennas. This correlation persists if the spacecraft is rotated such that the X-antenna is no longer aligned with the density gradient. Each of the waveform envelope minima on the X-antenna (for example, A and C in Figure 5) correspond to zero crossings of Re[E_X] in Figure 4. Similarly, the envelope minima on the Y antenna correspond to zero crossings of Re[E_Y] in Figure 4. The zero crossings on the X antenna in Figure 4 correlate with the extrema on the Y antenna (and vice versa) within the constant density region ($X < 0$). This appears to be a general property, even for

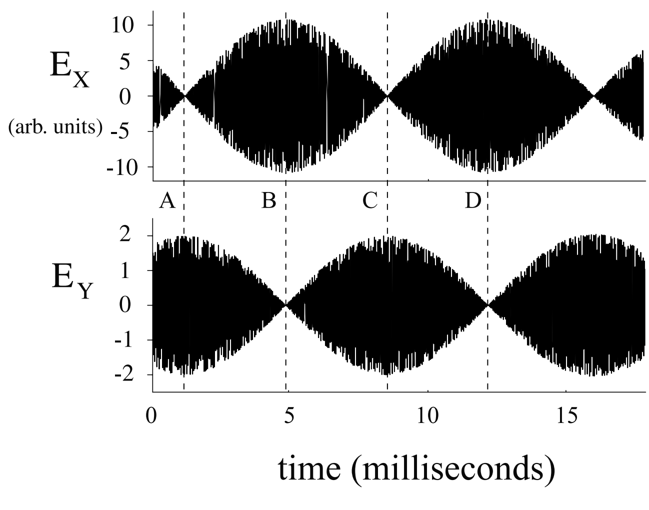

Figure 5. Predicted electric field $\mathbf{E}(t)$ on X and Y antennas, for spacecraft trajectory defined by equations (19) and (20), with $X_0 = -1$, $Y_0 = 0$, $\theta_{sc} = \pi/8$, $\phi_{sc} = \pi/16$, and assuming that the X-antenna is aligned with the density gradient.

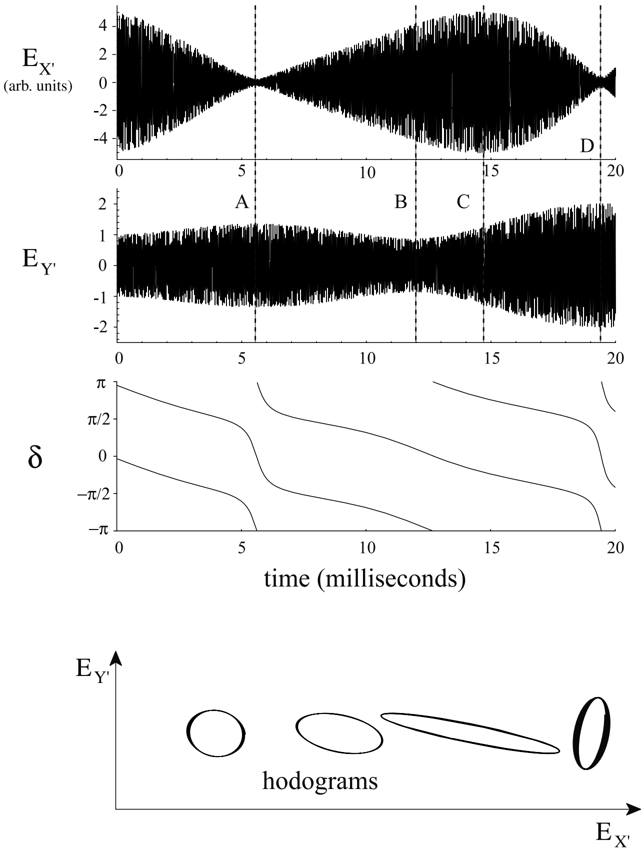

Figure 6. Predicted electric field $\mathbf{E}(t)$ on X and Y antennas, relative phase δ, and hodograms (instantaneous trace of $\mathbf{E}$ over several wave periods), for $X_0 = 5.75$, $Y_0 = 0$, $\theta_{sc} = \pi/8$, $\phi_{sc} = \pi/16$. The X-antenna is rotated by $\pi/16$ away from the density gradient.

spatially varying density profiles, based on numerical results from numerous density profiles and a wide range of parameters.

[21] This correlation breaks down in evanescent regions, as is evident in Figure 4, for $X > 0$. Accordingly, the alignment of envelope maxima and minima on orthogonal antennas breaks down within, or in the vicinity of evanescent regions (where $N(X) > 1$). An example is shown in Figure 6, for a 20 ms "snapshot", corresponding to the range $X = 5.75$ to $X = 7.25$ in Figure 4. This includes the second evanescent region through which the Langmuir waves tunnel. For the waveforms displayed in Figure 6, the spacecraft is rotated by an arbitrary angle ($\pi/16$) about the Z-axis, so that the X-axis is no longer aligned with the density gradient. While the maxima/minima correlation is evident at times A and D (distant from the evanescent region), this correspondence clearly breaks down at times B and C, corresponding to the period in which the Langmuir waves tunnel through the evanescent region. Figure 6 exhibits all of the features displayed in Figure 5 of *Bale et al.* [1998]; namely, the shape of the waveform envelopes is different between the two antennas, and the relative phase and hodogram ellipticity vary with time.

[22] Based on these results, one interpretation of the transformation from regular waveforms (with similar envelope shapes and correlated maxima/minima) in the TDS event in Figure 3 (at times A and B) to more irregular waveforms (times C and D), is that the spacecraft enters an evanescent region between times B and C.

4. Mode Conversion

[23] A necessary condition for partial conversion of Langmuir waves to transverse electromagnetic waves is that the Langmuir wave incidence angle (relative to the density gradient) is small. For the solar wind parameters assumed in the previous section, this condition corresponds to $\theta_L < \theta_{L\,\max} = 0.011$ rad $= 0.63°$. Figure 7 displays the electric field component solutions to the wave equations, E_X and E_Y, for incident Langmuir wave angle $\theta_L = 9.5 \times 10^{-3}$ rad. The small incidence angle ensures that the magnitude of the perpendicular field is very small, with $|E_Y| \ll |E_X|$. The perpendicular field E_Y is predominantly the field of the electromagnetic wave, of which less than a quarter of a wavelength is visible in Figure 7, together with a smaller electrostatic component (periodic variation with electrostatic wavelength $\approx$1). In this example, approximately 20% of the incoming Langmuir wave energy is converted into transverse electromagnetic waves.

[24] Figure 8 shows components of the electric field $\mathbf{E}(t)$ measured on the X and Y antennas, for the $E(X)$ and $E(Y)$ fields in Figure 7, spacecraft trajectory angles $\theta_{sc} = \pi/8$ and $\phi_{sc} = \pi/16$, and assuming that the X-antenna is aligned with density gradient. As in the total reflection regime (section 3), the correlation of envelope maxima and minima on orthogonal antennas is maintained away from evanescent regions. A significant difference from the total reflection case is that the relative phase slowly varies, with average relative phase $\langle\delta\rangle \neq \pm\pi/2$. For example, in Figure 8 the average phase $\langle\delta\rangle \approx -\pi/4$, $3\pi/4$, whereas for total reflection the relative phase between the two antennas satisfies $\delta = \pm\pi/2$. The average phase drifts over a timescale corresponding to the transverse wavelength (see Figure 7), and is approximately constant over the TDS "snapshot"

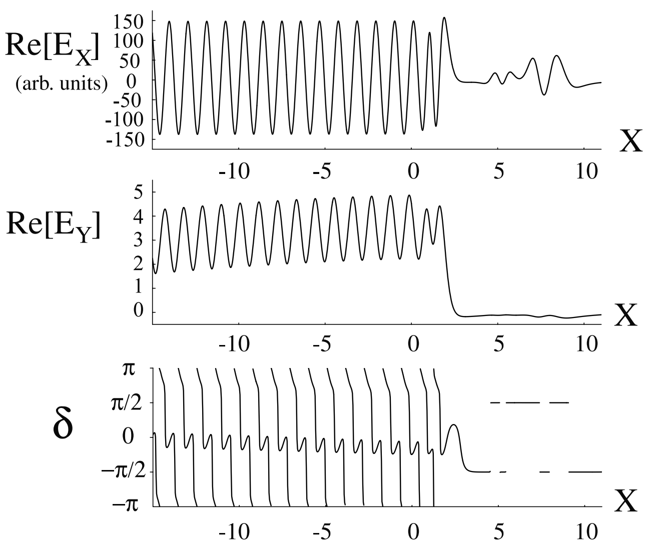

Figure 7. Electric field components $\mathrm{Re}[E_X(X)]$ and $\mathrm{Re}[E_Y(X)]$, and relative phase δ for incident Langmuir wave angle $\theta_L = 9.5 \times 10^{-3}$ rad.

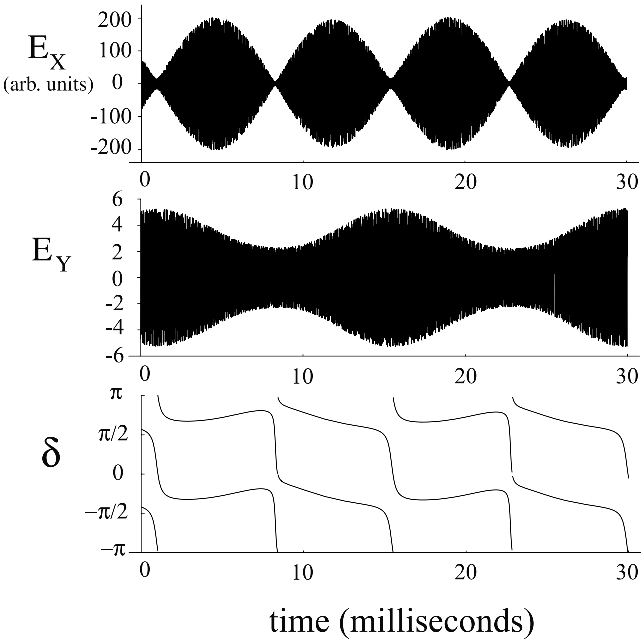

Figure 8. Predicted electric fields on X and Y antennas, and relative phase δ for same parameters as in Figure 7, for $X_0 < 0$ (i.e., in the constant density region), $Y_0 = 0$, $\theta_{sc} = \pi/8$, $\phi_{sc} = \pi/16$, and the X-antenna aligned with the density gradient.

timescale (17 ms). The combination of nearly constant average relative phase, with values $\langle\delta\rangle \neq \pm\pi/2$, and low fields on one antenna, with $E_Y/E_X \lesssim \theta_{L\,\max}$, thus constitutes a signature of mode conversion. However, for mode conversion to be detected in this way in practice requires that one antenna (say, the Y-antenna) is almost exactly aligned perpendicular to the density gradient. Otherwise, even small deviations from this configuration results in the Y-antenna primarily detecting the high electric field parallel to the density gradient (E_X in Figure 7), and zero relative phase shift between the two antennas. Our preliminary search of the Wind TDS data set confirms that unambiguous mode conversion events are extremely rare.

5. Discussion and Conclusions

[25] The main result in this paper is the demonstration that Langmuir wave tunneling in evanescent regions, where the local plasma frequency (which varies with density inhomogeneities in the plasma) exceeds the Langmuir wave frequency, produces different Langmuir waveform envelopes on two orthogonal spacecraft antennas. Outside evanescent regions, beating between incident and reflected Langmuir waves produce correlated waveform envelopes on the two antennas. According to this interpretation, the frequent detection of irregular Langmuir waveforms on two antennas by the Wind spacecraft [*Bale et al.*, 1998; *Kellogg et al.*, 1999] thus indicates that evanescent regions are common in the solar wind and foreshock plasmas. In contrast, Langmuir wave reflection at density gradients [*Kellogg et al.*, 1999] and nonlinear Langmuir wave decay [*Cairns and Robinson*, 1992b] predict regular beating with correlated waveforms on orthogonal antennas, which is also often observed. Similarly, single-antenna Langmuir waveforms detected by Voyager and Galileo which are inconsistent with regular beating [*Gurnett et al.*, 1981, 1993; *Hospodarsky et al.*, 1994] can also be explained in the context of evanescent tunneling. For instance, solitary Langmuir wave packets correspond to Langmuir waves trapped between two closely spaced evanescent regions. The prevalence of evanescent regions has important implications for the growth and scattering of Langmuir waves.

[26] This analysis assumes a preexisting and time-invariant flux of incoming Langmuir waves, and does not treat Langmuir wave interactions with beam electrons (i.e., wave growth and localization effects). Kinetic localization of Langmuir waves [*Muschietti et al.*, 1995, 1996] and stochastic growth [*Robinson et al.*, 1993a, 1993b; *Cairns and Robinson*, 1999] may occur in addition to tunneling and contribute to the irregularity of the Langmuir waveforms.

[27] The process of partial mode conversion of Langmuir waves to transverse electromagnetic waves occurs within a narrow range of incidence angles to the density gradient. This process has a unique dual-antenna signature, which can only be detected by orthogonal antennas when one antenna is aligned perpendicular to the density gradient, thus avoiding the dominant longitudinal electric field signal parallel to the density gradient. No unambiguous mode conversion events have yet been detected by this method, though a more complete search of the Wind data set is planned for future research.

[28] An important limitation of this analysis is the assumption that the plasma is unmagnetized. Even though the solar wind plasma is very weakly magnetized at 1 AU (with $\Omega_e/\omega_p \lesssim 0.01$), there is strong evidence to suggest that the weak magnetization has important implications on the properties of the Langmuir waves. *Bale et al.* [1998] reported that the average phase shift between orthogonal antennas varies with the angle between the antennas and the interplanetary magnetic field direction. Explanation of this phenomenon requires the extension of this analysis to include the effects of a weak magnetic field.

[29] **Acknowledgments.** This research was funded by the University of Sydney and the Australian Research Council, and NASA grants NAG5-6369 and NAG5-6127.

[30] Shadia Rifai Habbal thanks Paul J. Kellogg and another referee for their assistance in evaluating this paper.

References

Bale, S. D., D. Burgess, P. J. Kellogg, K. Goetz, and S. J. Monson, On the amplitude of intense Langmuir waves in the terrestrial electron foreshock, *J. Geophys. Res.*, *102*, 11,281, 1997.

Bale, S. D., P. J. Kellogg, K. Goetz, and S. J. Monson, Transverse *z*-mode waves in the terrestrial electron foreshock, *Geophys. Res. Lett.*, *25*, 9, 1998.

Cairns, I. H., A theory for the Langmuir waves in the electron foreshock, *J. Geophys. Res.*, *92*, 2329, 1987.

Cairns, I. H., and P. A. Robinson, Strong Langmuir turbulence at Jupiter?, *Geophys. Res. Lett.*, *19*, 1069, 1992a.

Cairns, I. H., and P. A. Robinson, Theory for low-frequency modulated Langmuir wave packets, *Geophys. Res. Lett.*, *19*, 2187, 1992b.

Cairns, I. H., and P. A. Robinson, Inconsistency of Ulysses millisecond Langmuir spikes with wave collapse in type III radio sources, *Geophys. Res. Lett.*, *22*, 3437, 1995.

Cairns, I. H., and P. A. Robinson, Strong evidence for stochastic growth of Langmuir-like waves in Earth's foreshock, *Phys. Rev. Lett.*, *82*, 3066, 1999.

Field, G. B., Radiation by plasma oscillations, *Astophys. J.*, *124*, 555, 1956.

Filbert, P. C., and P. J. Kellogg, Electrostatic noise at the plasma frequency beyond the Earth's bowshock, *J. Geophys. Res.*, *84*, 2788, 1979.

Forslund, D. W., J. M. Kindel, K. Lee, E. L. Lindman, and R. L. Morse, Theory and simulation of resonant absorption in a hot plasma, *Phys. Rev. A*, *11*, 679, 1975.

Gurnett, D. A., J. E. Maggs, D. L. Gallagher, W. S. Kurth, and F. L. Scarf, Parametric interaction and spatial collapse of beam-driven Langmuir waves in the solar wind, *J. Geophys. Res.*, *86*, 8833, 1981.

Gurnett, D. A., G. B. Hospodarsky, W. S. Kurth, D. J. Williams, and S. J. Bolton, Fine structure of Langmuir waves produced by a solar electron event, *J. Geophys. Res.*, *98*, 5631, 1993.

Hinkel-Lipsker, D. E., B. D. Fried, and G. L. Morales, Analytic expressions for mode conversion in a plasma with a linear density profile, *Phys. Fluids B*, *4*, 559, 1992.

Hospodarsky, G. B., D. A. Gurnett, W. S. Kurth, M. G. Kivelson, R. J. Strangeway, and S. J. Bolton, Fine structure of Langmuir waves observed upstream of the bow shock at Venus, *J. Geophys. Res.*, *99*, 13,363, 1994.

Kellogg, P. J., Observations concerning the generation and propagation of Type III solar bursts, *Astron. Astrophys.*, *169*, 329, 1986.

Kellogg, P. J., K. Goetz, S. J. Monson, and S. D. Bale, Langmuir waves in a fluctuating solar wind, *J. Geophys. Res.*, *104*, 17,069, 1999.

Means, R. W., L. Muschietti, M. Q. Tran, and J. Vaclavik, Electromagnetic radiation from an inhomogeneous plasma: Theory and experiment, *Phys. Fluids*, *24*, 2197, 1981.

Muschietti, L., I. Roth, and R. E. Ergun, Kinetic localization of beam-driven Langmuir waves, *J. Geophys. Res.*, *100*, 17,481, 1995.

Muschietti, L., I. Roth, and R. E. Ergun, On the formation of wave packets in planetary foreshocks, *J. Geophys. Res.*, *101*, 15,605, 1996.

Robinson, P. A., I. H. Cairns, and D. A. Gurnett, Clumpy Langmuir waves in type III radio sources: Comparison of stochastic-growth theory with observations, *Astrophys. J.*, *407*, 790, 1993a.

Robinson, P. A., A. J. Willes, and I. H. Cairns, Dynamics of Langmuir and ion-sound waves in type III solar radio sources, *Astrophys. J.*, *408*, 720, 1993b.

Unti, T. W. J., M. Neugebauer, and B. E. Goldstein, Direct measurements of solar-wind fluctuations between 0.0048 and 13.3 Hz, *Astrophys. J.*, *180*, 591, 1973.

Willes, A. J., and I. H. Cairns, Generalized Langmuir waves in magnetized kinetic plasmas, *Phys. Plasmas*, *7*, 3167, 2000.

Willes, A. J., and I. H. Cairns, Mode-conversion and reflection of Langmuir waves in an inhomogeneous solar wind, *Publ. Astron. Soc. Aust.*, *18*, 355, 2001.

Yin, L., and M. Ashour-Abdalla, Mode conversion in a weakly magnetized plasma with a longitudinal density profile, *Phys. Plasmas*, *6*, 449, 1999.

S. D. Bale, Space Sciences Laboratory, University of California, Berkeley, CA 94720-7450, USA.

I. H. Cairns and A. J. Willes, School of Physics, University of Sydney, New South Wales, Australia 2006. (willes@physics.usyd.edu.au)